

Finite Difference Schemes for Incompressible Flows in the Velocity–Impulse Density Formulation

Weinan E¹

Courant Institute of Mathematical Sciences, New York University, New York, New York 10012

and

Jian-Guo Liu²

Department of Mathematics, Temple University, Philadelphia, Pennsylvania 19122

Received October 2, 1995; revised May 6, 1996

We consider finite difference schemes based on the impulse density variable. We show that the original velocity—impulse density formulation of Oseledets is marginally ill-posed for the inviscid flow, and this has the consequence that some ordinarily stable numerical methods in other formulations become unstable in the velocity—impulse density formulation. We present numerical evidence of this instability. We then discuss the construction of stable finite difference schemes by requiring that at the numerical level the nonlinear terms be convertible to similar terms in the primitive variable formulation. Finally we give a simplified velocity—impulse density formulation which is free of these complications and yet retains the nice features of the original velocity—impulse density formulation with regard to the treatment of boundary. We present numerical results on this simplified formulation for the driven cavity flow on both the staggered and non-staggered grids. © 1997 Academic Press

1. INTRODUCTION

Recently there has been a great deal of interest in using the impulse density variable as a numerical tool in the computation of incompressible flows. Most of these activities are centered around the vortex method [2, 3, 5, 8, 19]. Butke was the first to realize the potential advantage of implementing vortex method using the impulse density: the natural hamiltonian form, natural interpretation of the flow field in terms of vortex loops or dipoles, faster decay at infinity and the trivial incompressibility property when the flow field is decomposed into a collection of vortex loops. This last property provided the starting point for a new creation method which trivially enforces the divergence-free property [19]. We refer to [7] for a summary

¹ weinan@cims.nyu.edu. Research supported by a Sloan Foundation fellowship and NSF grant DMS-9303779.

² jliu@math.temple.edu. Research supported by NSF grant DMS-9505275.

together with perspectives on the application of real space renormalization procedures to vortex methods based on the impulse density.

At a first sight, the impulse density formulation also provides an attractive way of dealing with the issues of boundary conditions for numerical methods in the Eulerian frame, such as finite difference and spectral methods. Methods based on vorticity formulations have to face the issue of enforcing divergence-free conditions for velocity, vorticity, or the vector potential. Although in many cases easy solutions can be found (see for example [10]), this becomes a severe limitation on the flexibility of the vorticity formulation. The velocity-pressure formulation, on the other hand, works well on staggered grid. However, boundary condition is still an issue on non-staggered grids, particularly so when higher than second order methods are sought.

The velocity—impulse density formulation seems to provide a way of combining the nice features of the two formulations discussed above, and yet is free of the problems. There is no need to impose divergence-free property for the impulse density. The computed velocity is naturally divergence-free since it is the projection of the impulse density to the space of divergence-free vector fields. The boundary condition for the impulse density can be treated in the same way as the treatment of the vorticity boundary condition. This is much easier than the pressure boundary condition. In particular the velocity—impulse density formulation seems to provide an easy way of constructing numerical methods on non-staggered grids.

However as we report in Section 2, the impulse density formulation does have some serious flaws. For inviscid flows, the linearized equation is marginally ill-posed—it contains a non-trivial Jordan block (Similar observations were made in [5]). It is well-known [16] that at a numerical level this marginal ill-posedness can translate to a catastrophic instability of the numerical schemes. Indeed this is

observed in our computations. In Section 2 we will present numerical evidence that the standard Fourier—collocation methods and second order centered difference methods are unstable for the inviscid flow. Since both methods are stable in the primitive variable and vorticity-stream function formulations, this numerical instability is purely an artifact of the velocity—impulse density formulation. Although the viscous term does have a stabilizing effect, the instability for the inviscid problem imposes a severe constraint on the size of the cell Reynolds number which makes it essentially useless for high Reynolds number flows.

To avoid this instability we observe that the impulse density formulation is just another form of the Euler (or Navier–Stokes) equation which is well-posed. Therefore if the numerical methods can be converted to a stable scheme in the primitive variable formulation, then the instability should not be present in the original impulse density formulation either. In Section 3, we will discuss examples of finite difference methods such that this conversion is indeed possible at a discrete level. We will also present numerical evidence that these numerical schemes are indeed stable.

Although the recipe described in Section 3 does provide a solution to the instability problem, the whole procedure is unnecessarily complicated. In Section 4, we give an alternative formulation which retains the structure of the impulse density formulation except for the convective term which is taken to be the same as in the original Navier–Stokes equation. In this formulation, the potential numerical advantages of the impulse formulation mentioned earlier are kept, although the hamiltonian structure is lost. Since our primary purpose is the accurate approximation of the Navier–Stokes equation at transient time scales, the latter issue may mainly be cosmetic.

This new simplified formulation proves to be a very effective numerical tool for general geometries and general grids. It is closely related to the projection method [6, 20, 13, 21, 1] except that the issue of boundary condition for pressure is replaced by that of the gauge. The latter is much simpler to deal with. This and related topics will be discussed in a forthcoming paper.

2. MARGINAL ILL-POSEDNESS OF THE VELOCITY–IMPULSE DENSITY FORMULATION AND THE IMPLICATIONS FOR COMPUTATIONS

We will restrict ourselves to 2D. It is easy to see that our discussions are as relevant to 3D.

Building on earlier work of Roberts [17], Oseledets observed that the Navier–Stokes equations can be written in terms of a new variable \mathbf{M} :

$$\begin{cases} \partial_t \mathbf{M} + (\mathbf{u} \cdot \nabla) \mathbf{M} + \mathbf{M} \cdot (\nabla \mathbf{u})^\top = \frac{1}{\text{Re}} \Delta \mathbf{M}, \\ \mathbf{u} = \mathcal{P} \mathbf{M}, \end{cases} \quad (2.1)$$

where \mathbf{u} is the velocity field, \mathcal{P} is the L^2 projection operator to the space of divergence-free vector fields. The connection between (2.1) and the standard Navier–Stokes equation is as follows. If \mathbf{M} satisfies (2.1), and $\mathbf{M} = \mathbf{u} + \nabla \phi$, let

$$p = \partial_t \phi + (\mathbf{u} \cdot \nabla) \phi - \frac{1}{\text{Re}} \Delta \phi + \frac{1}{2} |\mathbf{u}|^2, \quad (2.2)$$

then (\mathbf{u}, p) satisfies the Navier–Stokes equation:

$$\begin{cases} \partial_t \mathbf{u} + (\mathbf{u} \cdot \nabla) \mathbf{u} + \nabla p = \frac{1}{\text{Re}} \Delta \mathbf{u}, \\ \nabla \cdot \mathbf{u} = 0, \end{cases} \quad (2.3)$$

Conversely if (\mathbf{u}, p) satisfies (2.3), let ϕ be a solution of (2.2) and $\mathbf{M} = \mathbf{u} + \nabla \phi$, then (\mathbf{M}, ϕ) is a solution of (2.1). The primary motivation of Oseledets was to write the incompressible Euler equation in a hamiltonian form. The simplest way is to use the Lagrangian coordinates $\{\alpha\}$: Let $\mathbf{x}(\alpha, t)$ be the position of a particle with Lagrangian coordinate α at time t , and $\mathbf{M}(\alpha, t)$ be the impulse density at that position. $\{\mathbf{x}(\alpha, t), \mathbf{M}(\alpha, t)\}$ should satisfy

$$\frac{d\mathbf{x}}{dt} = \frac{\delta H}{\delta \mathbf{M}}, \quad \frac{d\mathbf{M}}{dt} = -\frac{\delta H}{\delta \mathbf{x}}, \quad (2.4)$$

where $H = \frac{1}{2} \int |\mathbf{u}|^2 d\mathbf{x}$ is the total kinetic energy. One simple consequence of (2.1) is that the generalized helicity $\mathbf{M} \cdot \boldsymbol{\omega}$ ($\boldsymbol{\omega} = \nabla \times \mathbf{u}$) is conserved along particle path:

$$D_t(\mathbf{M} \cdot \boldsymbol{\omega}) = 0 \quad (2.5)$$

where $D_t = \partial_t + (\mathbf{u} \cdot \nabla)$ is the material derivative operator. Physically \mathbf{M} can be interpreted as a vortex dipole density (analog of magnetization) [4], or the impulse density [2].

2.1. Linearized Analysis for the Inviscid Case

Let us linearize (2.1) around a constant state $\bar{\mathbf{u}} = (\bar{u}, \bar{v})$ and $\bar{\mathbf{M}} = (\bar{M}, \bar{N})$. The linearized equations are

$$\begin{cases} \partial_t M + \bar{u} \partial_x M + \bar{v} \partial_y M + \bar{M} \partial_x \bar{u} + \bar{N} \partial_x \bar{v} = 0 \\ \partial_t N + \bar{u} \partial_x N + \bar{v} \partial_y N + \bar{M} \partial_y \bar{u} + \bar{N} \partial_y \bar{v} = 0 \\ \mathbf{u} = (u, v) = \mathcal{P} \mathbf{M}, \end{cases} \quad (2.6)$$

where $\mathbf{M} = (M, N)$. Transforming to Fourier space, we have

$$\begin{cases} \partial_t \hat{M} + i(\bar{u} k_1 + \bar{v} k_2) \hat{M} + i k_1 (\bar{M} \hat{u} + \bar{N} \hat{v}) = 0 \\ \partial_t \hat{N} + i(\bar{u} k_1 + \bar{v} k_2) \hat{N} + i k_2 (\bar{M} \hat{u} + \bar{N} \hat{v}) = 0 \end{cases} \quad (2.7)$$

and

$$\begin{pmatrix} \hat{u} \\ \hat{v} \end{pmatrix} = \left(I - \frac{\mathbf{k} \otimes \mathbf{k}}{|\mathbf{k}|^2} \right) \begin{pmatrix} \hat{M} \\ \hat{N} \end{pmatrix} \quad (2.8)$$

where $\mathbf{k} = (k_1, k_2)$, $\mathbf{k} \otimes \mathbf{k} = \mathbf{k}^T \mathbf{k}$.

We now look at the special case when $\bar{N} = 0$, $\bar{v} = 0$ and $k_1 = 0$, so (2.7) becomes

$$\begin{cases} \partial_t \hat{M} = 0 \\ \partial_t \hat{N} + ik_2 \bar{M} \hat{u} = 0 \end{cases} \quad (2.9)$$

From (2.8) we get $\hat{u} = \hat{M}$. Therefore (2.7) becomes

$$\partial_t \begin{pmatrix} \hat{M} \\ \hat{N} \end{pmatrix} + ik_2 \bar{M} \begin{pmatrix} 0 & 0 \\ 1 & 0 \end{pmatrix} \begin{pmatrix} \hat{M} \\ \hat{N} \end{pmatrix} = 0 \quad (2.10)$$

The matrix in (2.10) has a non-trivial Jordan block. This means that the Fourier modes grow linearly in t with a rate proportional to k_2 :

$$\hat{M}(\mathbf{k}, t) = \hat{M}(\mathbf{k}, 0), \quad \hat{N}(\mathbf{k}, t) = \hat{N}(\mathbf{k}, 0) - ik_2 t \bar{M} \hat{M}(\mathbf{k}, 0). \quad (2.11)$$

Therefore the linearized equations are marginally ill-posed.³

In her thesis [5] M. Chen made the observation that upon linearization the matrix has two coinciding eigenvalues but only one eigenvector. This is another form of stating the problem is linearly marginally ill-posed.

2.2. Implications for Computations

It is well-known that lower order perturbations can turn this marginal ill-posedness into catastrophic ill-posedness, i.e. Fourier modes grow exponentially with rates unbounded in the wavenumber space [16]. Such lower order terms can come from the variable—coefficient (actually nonlinear) nature of the problem. Consequently an ordinarily stable scheme in other formulations can become unstable in the impulse density formulation. This is indeed observed in our numerical computations.

Below we report the numerical results for two standard numerical methods, a Fourier-collocation method with smooth filter and a second order centered difference scheme. We choose the well-known test problem of a jet with initial data

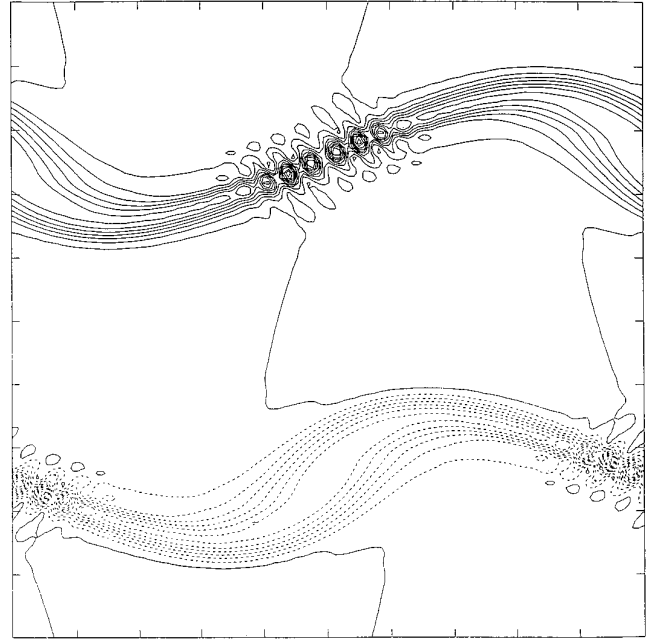


FIG. 1. Contour plot of vorticity at $t = 1/\pi$ computed by the Fourier-collocation method. This figure shows the onset of the numerical instability.

$$u(x, y) = \begin{cases} \tanh((y - 0.25)/\rho) & \text{for } y \leq 0.5 \\ \tanh((0.75 - y)/\rho) & \text{for } y > 0.5 \end{cases} \quad (2.12)$$

$$v(x, y) = \delta \sin(2\pi x)$$

where $\rho = 1/(10\pi)$ and $\delta = 0.25$. This test problem is often used because it is practically periodic in both x and y directions. We always take $\phi(\cdot, 0) = 0$.

We first report the result of the Fourier method. This is the standard Fourier-collocation method, coupled with classical Runge–Kutta in time, and a smooth filter when computing derivatives. The details of that filter is described in [11] where the same method was used in the primitive variable formulation to compute the same problem and the numerical results were used as benchmarks to test the ENO method. Although we carried out the numerical test on a variety of grid sizes, the numerical phenomena we observed is insensitive to the size of the grid. Hence we will only report the results on the 128^2 grid.

Figure 1 is the contour plot of vorticity at $t = 1/\pi$ when the numerical instability characterized by the small scale structures is becoming apparent. The development of the numerical instability is most clearly seen from Figure 2 which shows the time evolution of the energy spectrum of \mathbf{M} . The accumulation of energy at small scales is evident. This eventually leads to an catastrophic explosion at $t = 1.25/\pi$. Note that a similar method (actually a small modification of the code) based on the primitive variables runs well up to much later times until accuracy is lost.

³ This is also referred to as being weakly well-posed [16].

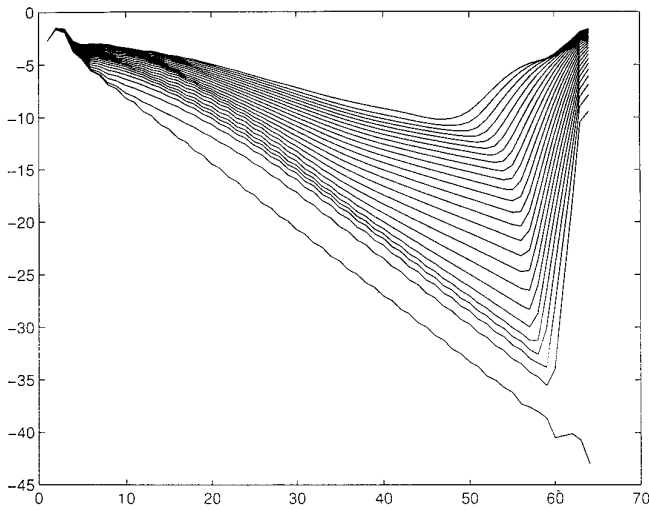


FIG. 2. Time evolution of the energy spectrum of \mathbf{M} at times: $t = 0.05/\pi, 0.1/\pi, 0.15 \cdot \pi \cdots 1.2/\pi$. Time increases upward. Log of the energy spectrum is plotted.

Next we discuss the numerical results from a standard centered difference method. At a semi-discrete level the method can be described as:

$$\begin{cases} \partial_t \mathbf{M} + (\mathbf{u} \cdot \nabla_h) \mathbf{M} + \mathbf{M} \cdot (\nabla_h \mathbf{u})^\top = \frac{1}{\text{Re}} \Delta_h \mathbf{M}, \\ \Delta_h \phi = \nabla_h \cdot \mathbf{M}, \\ \mathbf{u} = \mathbf{M} - \nabla_h \phi \end{cases} \quad (2.13)$$

where ∇_h is the standard centered difference operator, and Δ_h is the standard 5-point formula for the Laplacian. We use classical Runge–Kutta to discretize time.

Figure 3 is the analog of Figure 1 for this centered scheme. It is at an earlier time since the method is less accurate than the Fourier method, therefore errors kick in earlier. As in the case of the Fourier method, this error is quickly amplified, leading to a catastrophic explosion. We do not show the energy spectrum here since it is very similar to Figure 2.

As expected the viscous term does provide a stabilizing factor for this numerical instability. However the limit on the Reynolds number is rather severe. On a 128^2 grid we found that stable numerical results can be expected up to time $t = 1.5/\pi$ for $\text{Re} < 650$ for the second order scheme, and $\text{Re} < 1250$ for the Fourier-collocation method. An example of such result is shown in Figure 4. It is important to realize that this limitation comes from stability considerations rather than accuracy.

3. STABLE FINITE DIFFERENCE METHODS IN THE VELOCITY–IMPULSE DENSITY FORMULATION

The numerical instability discussed in the last section is purely an artifact of the formulation—the original incom-

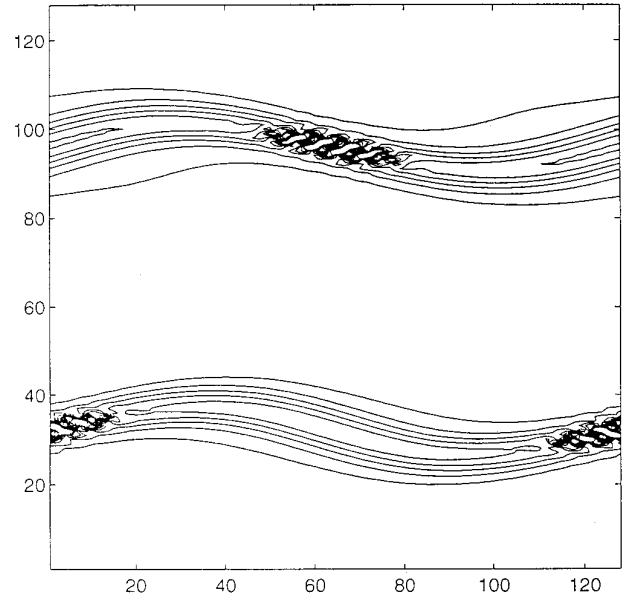


FIG. 3. Contour plot of vorticity computed using the centered scheme at $t = 0.17$ showing the onset of numerical instability.

pressible Euler’s equation is well-posed. Therefore a simple idea for constructing stable numerical methods using impulse density is to require that the method be convertible to the primitive variable form. This is the discrete analog of the relation between (2.1) and (2.3). In this section, we

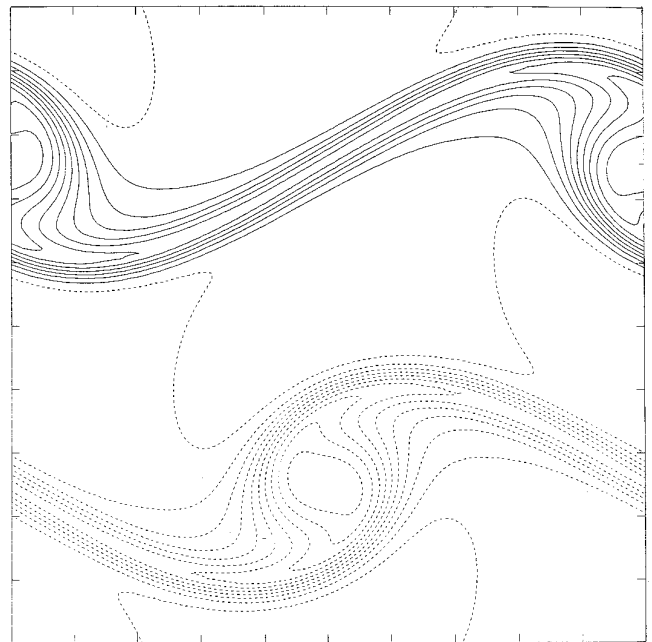


FIG. 4. Contour plot of vorticity at Reynolds number 1250 computed using the Fourier-collocation method. $t = 1.5/\pi$.

show that in this way it is indeed possible to construct stable schemes based on the impulse density variable.

Let us concentrate on the first component of the dynamic equation and use the notation $\mathbf{M} = (M, N)$, $\mathbf{u} = (u, v)$. Consider the scheme:

$$\partial_t M + \bar{u}D_x M + \bar{v}D_y M + \overline{M}D_x u + \overline{N}D_x v = 0 \quad (3.1)$$

We will specify the overbar, D_x , D_y , G_x , G_y operators later. Substituting in

$$M = u + G_x \phi, \quad N = v + G_y \phi \quad (3.2)$$

and rearranging terms, we get

$$\partial_t u + \bar{u}D_x u + \bar{v}D_y u + G_x(\partial_t \phi) + I_2 + I_3 = 0 \quad (3.3)$$

where

$$I_2 = \bar{u}D_x G_x \phi + \bar{v}D_y G_x \phi + \overline{G_x \phi}D_x u + \overline{G_y \phi}D_x v \quad (3.4)$$

$$I_3 = \bar{u}D_x u + \bar{v}D_x v \quad (3.5)$$

We require that $I_2 + I_3$ be the first component of a discrete gradient term: (2.2) suggests that we should expect

$$I_2 = G_x(\bar{u}D_x \phi + \bar{v}D_y \phi), \quad I_3 = \frac{1}{2}G_x(u^2 + v^2) \quad (3.6)$$

EXAMPLE 1. Let D_x , D_y , G_x , G_y be the standard centered difference operators. Define $\bar{f}_{i,j} = \frac{1}{2}(f_{i+1,j} + f_{i-1,j})$. For the second component of the dynamic equation, the overbar operator has to be defined as $\bar{f}_{i,j} = \frac{1}{2}(f_{i,j+1} + f_{i,j-1})$. Then we have

$$\begin{aligned} I_3 &= \frac{1}{2}(u_{i+1,j} + u_{i-1,j}) \frac{u_{i+1,j} - u_{i-1,j}}{2 \Delta x} \\ &\quad + \frac{1}{2}(v_{i+1,j} + v_{i-1,j}) \frac{v_{i+1,j} - v_{i-1,j}}{2 \Delta x} \\ &= \frac{1}{4 \Delta x} (u_{i+1,j}^2 - u_{i-1,j}^2 + v_{i+1,j}^2 - v_{i-1,j}^2) \\ &= \frac{1}{2}(G_x(u^2 + v^2))_{i,j} \end{aligned} \quad (3.7)$$

$$I_2 = \bar{u}D_x G_x \phi + \overline{G_x \phi}D_x u + \bar{v}D_x G_y \phi + \overline{G_y \phi}D_x v \quad (3.8)$$

Using the discrete product rule:

$$\bar{f}D_x g + \bar{g}D_x f = D_x(fg) \quad (3.9)$$

and the commutation relation

$$D_y G_x = D_x G_y \quad (3.10)$$

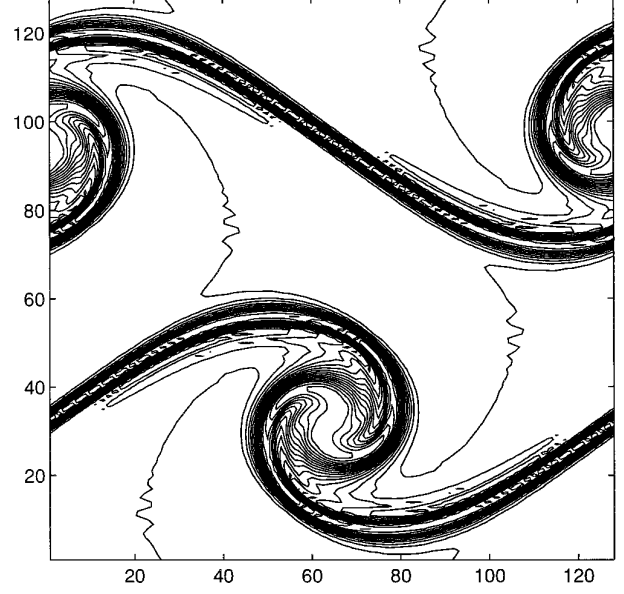


FIG. 5. Contour plot of vorticity computed using the stable second order centered difference method discussed in Section 3. Other numerical parameters are the same as the ones in Figure 4 except $t = 2/\pi$.

we get

$$I_2 = D_x(uG_x \phi + vG_y \phi) = G_x(uD_x \phi + vD_y \phi) \quad (3.11)$$

Finally we can rewrite (3.1) as

$$\begin{aligned} \partial_t u + \bar{u}D_x u + \bar{v}D_y u \\ + G_x \left(\partial_t \phi + uD_x \phi + vD_y \phi + \frac{1}{2}(u^2 + v^2) \right) = 0 \end{aligned} \quad (3.12)$$

Similarly the second component of the dynamic equation can be rewritten as

$$\begin{aligned} \partial_t v + \bar{u}D_x v + \bar{v}D_y v \\ + G_y \left(\partial_t \phi + uD_x \phi + vD_y \phi + \frac{1}{2}(u^2 + v^2) \right) = 0 \end{aligned} \quad (3.13)$$

Notice that the overbar operator in (3.12) and (3.13) are defined differently.

The only difference between this scheme and the one discussed in Section 2.2 is the treatment of the nonlinear terms. We have checked numerically that the directional averaging operation does make the scheme stable. In Figure 5 we show the numerical result computed using this new scheme. Other numerical parameters are the same as the ones in Figure 3 except that Figure 5 is at a later time. In contrast to Figure 3, we see no signs of numerical instability. The computation was carried out to longer time

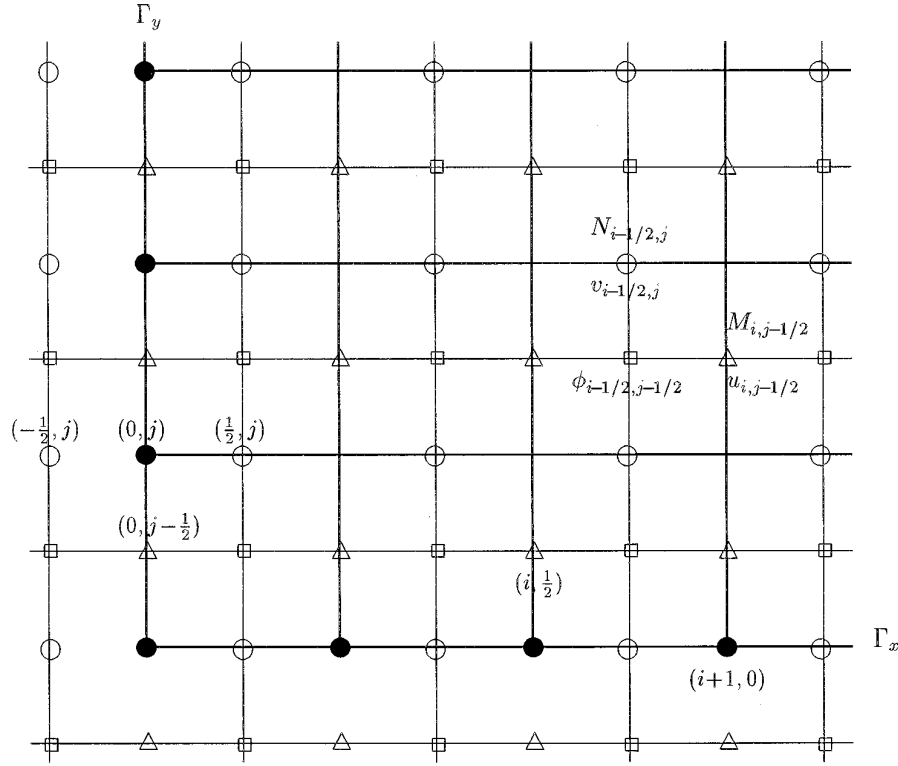


FIG. 6. Staggered grid, dark circles denote the grid points of the background grid at the boundary.

until accuracy was eventually lost due to thinning of the shear layers.

EXAMPLE 3. Let D_x , D_y , G_x , G_y be the standard forward difference operators. Define $\bar{f}_{i,j} = \frac{1}{2}(f_{i+1,j} + f_{i,j})$. For the second component of the dynamic equation, the over-bar operator has to be defined as $\bar{f}_{i,j} = \frac{1}{2}(f_{i,j+1} + f_{i,j})$. Then (3.1) can be rewritten as

$$\begin{aligned} \partial_t u + \bar{u} D_x u + \bar{v} D_y u + G_x(\partial_t \phi + u D_x \phi) \\ + v D_y \phi + \frac{1}{2}(u^2 + v^2) = 0 \end{aligned} \quad (3.14)$$

Similarly for the second component of the dynamic equation. We will not report any numerical results on this scheme since it is only first order accurate.

4. A SIMPLIFIED VELOCITY-IMPULSE DENSITY FORMATION

The complications discussed in Sections 2 and 3 come from the nonlinear terms. We saw in Section 2 that the nonlinear terms, as was written in the original velocity—impulse density formulation (2.1), easily trigger numerical instabilities. The cure to this instability discussed in Section 3 was to make sure that at a numerical level, the nonlinear

terms can also be converted to the corresponding terms in the primitive variable formulation.

All these complications become unnecessary if we just modify the velocity—impulse density formulation such that the nonlinear terms retain their original form in the primitive variable form. The modified velocity—impulse density formulation takes the form:

$$\begin{cases} \partial_t \mathbf{M} + (\mathbf{u} \cdot \nabla) \mathbf{u} = \frac{1}{\text{Re}} \Delta \mathbf{M} \\ \mathbf{u} = \mathcal{P} \mathbf{M} \end{cases} \quad (4.1)$$

If we write $\mathbf{M} = \mathbf{u} + \nabla \phi$, then pressure is given by

$$p = \partial_t \phi - \frac{1}{\text{Re}} \Delta \phi \quad (4.2)$$

This formation is actually simpler than (2.1) in many ways. Certainly the construction of stable numerical methods is much simpler. This will be discussed below. One important fact is that the potential advantage of the original velocity—impulse density formulation (2.1) with regard to the treatment of boundary condition is still retained. This can

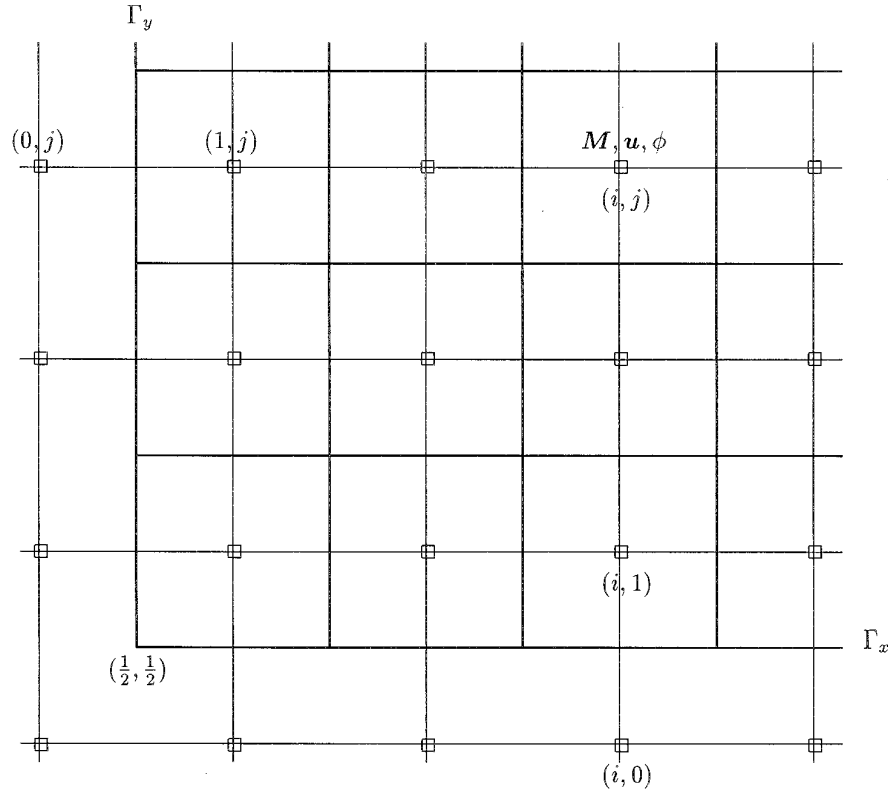


FIG. 7. Non-staggered grid.

be seen from 4.2 when we discuss finite difference schemes on non-staggered grids.

4.1. Finite Difference Methods Based on the Simplified Velocity–Impulse Density Formulation on Staggered Grid

We first demonstrate the application of the simplified velocity—impulse density formulation on the staggered grid—also referred to as the MAC grid. One such grid is displayed in Figure 6 where the gauge variable ϕ is defined at “□” points, the first and second component of the velocity u and v are defined at “△” and “○” points respectively; similarly for the impulse density. We can write the difference scheme as

$$\begin{cases} \partial_t M + u \tilde{D}_x u + E_x E_y v \tilde{D}_y u = \nu \Delta_h M, & \text{at “△” points,} \\ \partial_t N + E_x E_y u \tilde{D}_x v + v \tilde{D}_y v = \nu \Delta_h N, & \text{at “○” points,} \end{cases} \quad (4.3)$$

$$\Delta_h \phi = D_x M + D_y N, \quad \text{at “□” points.} \quad (4.4)$$

$$\begin{cases} u = M - D_x \phi, & \text{at “△” points,} \\ v = N - D_y \phi, & \text{at “○” points,} \end{cases} \quad (4.5)$$

where we used the notations

$$\begin{aligned} \Delta_h u &= (D_x^2 + D_y^2)u, \\ \tilde{D}_x u(x, y) &= \frac{u(x + \Delta x, y) - u(x - \Delta x, y)}{2 \Delta x}, \\ D_x u(x, y) &= \frac{u(x + \Delta x/2, y) - u(x - \Delta x/2, y)}{\Delta x}, \\ E_x u(x, y) &= \frac{u(x + \Delta x/2, y) + u(x - \Delta x/2, y)}{2}, \end{aligned}$$

and similarly for $\tilde{D}_y u$, $D_y u$, $E_y u$.

Now we come to the boundary conditions. The idea is to realize the boundary conditions for (u, v) through boundary conditions for (M, N) and ϕ . The simplest way of implementing the velocity boundary conditions in the MAC scheme is to use the reflection technique. On the segment Γ_x (see Figure 6), the boundary condition $v = 0$

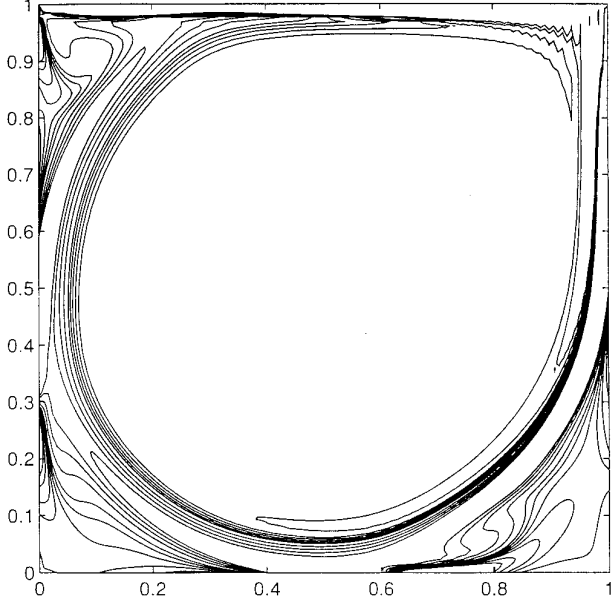


FIG. 8. Driven cavity flow at Reynolds number 10^4 , $t = 1000$. Shown here is the contour plot of vorticity at $t = 1000$ computed using the method described in Section 4.1 on the staggered grid.

is imposed exactly at the “○” points: $v_{i-1/2,0} = 0$, the boundary condition $u = 0$ is imposed approximately at the “●” points by letting

$$u_{i,-1/2} = -u_{i,1/2}. \quad (4.6)$$

Similarly on Γ_y , we have

$$v_{-1/2,j} = -v_{1/2,j}, \quad u_{0,j-1/2} = 0. \quad (4.7)$$

An easy way of realizing these boundary conditions is to impose Neumann boundary condition for ϕ ,

$$\phi_{i,-1/2} = \phi_{i,1/2} \quad \text{on } \Gamma_x, \quad \phi_{-1/2,j} = \phi_{1/2,j} \quad \text{on } \Gamma_y; \quad (4.8)$$

Once ϕ is known, the boundary condition for (M, N) can be obtained using (4.5). This means that on Γ_x we impose $N_{i-1/2,0} = 0$ at the “○” points, and

$$M_{i,-1/2} = -u_{i,1/2} + D_x \phi_{i,1/2}, \quad (4.9)$$

at the “●” points. Similarly on Γ_y , we have

$$N_{-1/2,j} = -v_{1/2,j} + D_y \phi_{1/2,j}, \quad M_{0,j-1/2} = 0. \quad (4.10)$$

Finally we mention that in the calculations presented below, time-stepping is done using the explicit 3rd or 4th order Runge–Kutta method. The details and advantages of this is discussed in [9].

4.2. Non-Staggered Grids

Now we discuss a method on non-staggered grid (see Figure 7). We define all the variables at the center of each computational cell, i.e. the “□” points. The momentum equations are discretized at these points using:

$$\begin{cases} \partial_t M + u \tilde{D}_x u + v \tilde{D}_y u = \nu \Delta_h M, \\ \partial_t N + u \tilde{D}_x v + v \tilde{D}_y v = \nu \Delta_h N. \end{cases} \quad (4.11)$$

The difference operators were defined earlier.

Next we discuss the implementation of the projection step. Following an idea of Rhie and Chow [15], we will compute discrete divergences by defining volume fluxes at the edges of the cells, e.g.

$$\begin{cases} M_{i+1/2,j} = (E_x M)_{i+1/2,j}, & \text{at “}\Delta\text{” points,} \\ N_{i,j+1/2} = (E_y N)_{i,j+1/2}, & \text{at “}\circ\text{” points,} \end{cases} \quad (4.12)$$

To define this at the boundary we need the values $\{M_{0,j}\}$ near Γ_x and $\{N_{i,0}\}$ near Γ_y which we define using the reflection technique:

$$M_{0,j} = -M_{1,j} \quad \text{on } \Gamma_y, \quad N_{i,0} = -N_{i,1} \quad \text{on } \Gamma_x \quad (4.13)$$

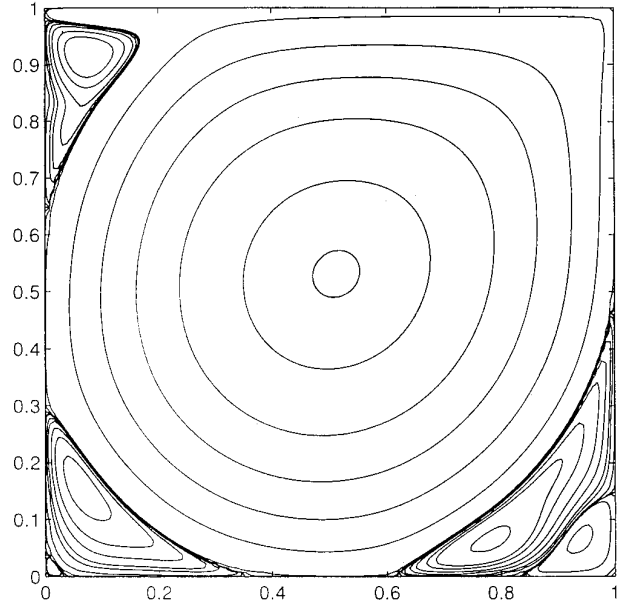


FIG. 9. Driven cavity flow at Reynolds number 10^4 , $t = 1000$. Shown here is the contour plot of stream function at $t = 1000$ computed using the method described in Section 4.1 on the staggered grid.

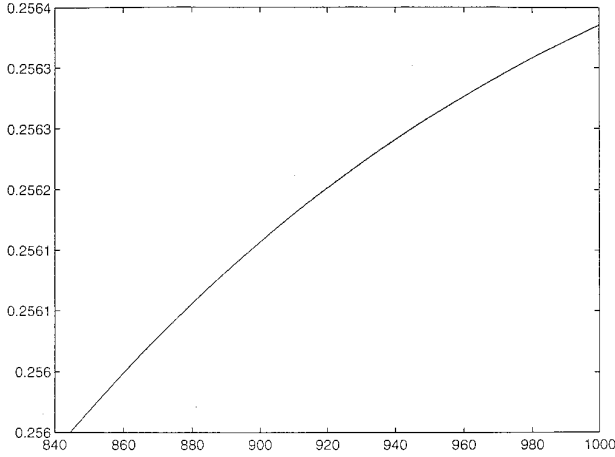


FIG. 10. Time history of total kinetic energy for the computations shown in Figures 8–9.

Divergence at the center of a cell (the “□” points) can now be defined as

$$\begin{aligned} (\operatorname{div} M)_{i,j} &= \frac{M_{i+1/2,j} - M_{i-1/2,j}}{\Delta x} + \frac{N_{i,j+1/2} - N_{i,j-1/2}}{\Delta y} \quad (4.14) \\ &= D_x(E_x M) + D_y(E_y N) = \tilde{D}_x M + \tilde{D}_y N. \end{aligned}$$

ϕ can be solved using

$$\Delta_h \phi = D_x(E_x M) + D_y(E_y N) = \tilde{D}_x M + \tilde{D}_y N, \quad (4.15)$$

and the Neumann condition:

$$\phi_{i,0} = \phi_{i,1} \quad \text{on } \Gamma_x, \quad \phi_{0,j} = \phi_{1,j} \quad \text{on } \Gamma_y. \quad (4.16)$$

This gives us naturally the mass fluxes at the edges of the cell:

$$\begin{aligned} u_{i+1/2,j} &= M_{i+1/2,j} - (D_x \phi)_{i+1/2,j}, & \text{at “}\triangle\text{” points,} \\ v_{i,j+1/2} &= N_{i,j+1/2} - (D_y \phi)_{i,j+1/2}, & \text{at “}\circ\text{” points,} \end{aligned} \quad (4.17)$$

which obey volume conservation on each cell:

$$(u_{i+1/2,j} - u_{i-1/2,j})/\Delta x + (v_{i,j+1/2} - v_{i,j-1/2})/\Delta y = 0. \quad (4.18)$$

We can now define the velocity at the center of the cell by take averages:

$$u_{i,j} = \frac{1}{2}(u_{i+1/2,j} + u_{i-1/2,j}), \quad v_{i,j} = \frac{1}{2}(v_{i,j+1/2} + v_{i,j-1/2}). \quad (4.19)$$

This completes the projection step.

Finally the tangential component of the impulse density at the boundary is obtained by:

$$M_{i,0} = -M_{i,1} + 2D_x \phi_{i,1}, \quad (4.20)$$

on Γ_x , and

$$N_{0,j} = -N_{1,j} + 2D_y \phi_{1,j}, \quad (4.21)$$

on Γ_y . In the end we have, for velocity at the boundary:

$$u_{i,0} = -u_{i,1}, \quad v_{i,0} = -v_{i,1}, \quad (4.22)$$

on Γ_x , and

$$u_{0,j} = -u_{1,j}, \quad v_{0,j} = -v_{1,j}, \quad (4.23)$$

on Γ_y . Again for time-stepping, we used explicit 3rd or 4th order Runge–Kutta methods.

We implemented these methods on a canonical test problem—the driven cavity flow. Again all computations were done on a 128^2 grid. The computational domain is $[0, 1] \times [0, 1]$. The boundary condition $u = 0, v = 0$ is imposed everywhere at the boundary except at $\{y = 1\}$ where we impose $u = 1, v = 0$. We will present the results at Reynolds number $\operatorname{Re} = 10^4$ which is the most extensively studied case [12, 18, 9]. With the exception of [9], other existing results were computed using the steady state equa-

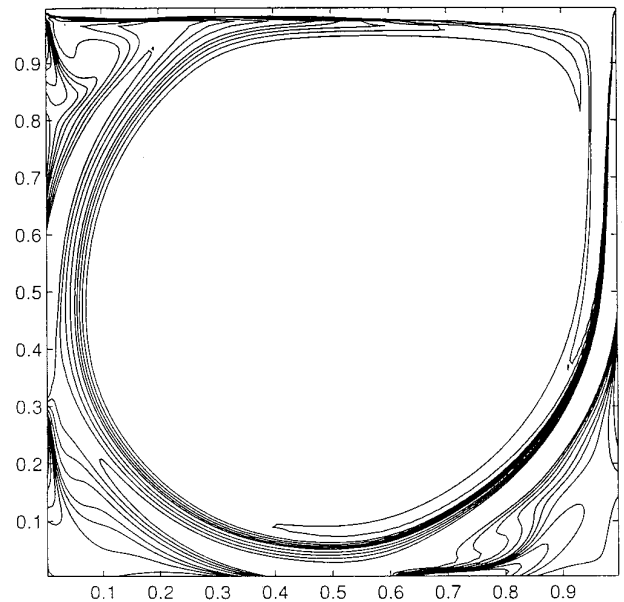


FIG. 11. Same as in Figure 8, but computed on the non-staggered grid.

tions directly. In particular, [12] contains accurate solutions of the steady Navier–Stokes equation using the multi-grid method. Here we will compute faithfully the unsteady dynamics in order to address the issue of whether the solutions of the unsteady Navier–Stokes equations converge to the steady state. At the present time, this is still an open question. For initial data we choose the impulsive start: $u = 0, v = 0$.

Figure 8 is the contour plot of vorticity computed using the method described in Section 4.1 at $t = 1000$. Aside from the small oscillations at the upper right corner, the numerical solution is almost indistinguishable from the steady state solutions in [12, 18]. Figure 9 shows that contour plot of stream function. Compared with the very accurate results of [12] computed on a 256^2 grid, we see that all the small scale features are reproduced. Another strong indication that the numerical solution is reaching steady state is given in Figure 10 where we plot the time history of energy. At the time when we stopped our computation, the total energy is only changing in its fifth digit. Similarly in Figure 11 we show the numerical results for the same problem using the non-staggered grid method described in Section 4.2. The same things as we said above apply to this case. In fact, we omit the plot for the time history of energy since it is virtually indistinguishable from Figure 10.

CONCLUDING REMARKS

Our impulse density-velocity formulation is very close to the formulation on which projection methods are based. The only difference is that we work with the gauge instead of the pressure. It turns out that this difference has drastic consequences in terms of numerical computations since we can use the freedom in selecting the gauge to simplify the issue of boundary conditions. This simplification makes it trivial to formulate efficient and even high order accurate projection-like methods on non-staggered grids. It also simplifies the theory and analysis of such projection methods. These topics will be discussed in a forthcoming paper.

REFERENCES

1. J. B. Bell, P. Collela, and H. G. Glaz, *J. Comput. Phys.* **85**(1989), pp. 257–283.
2. T. Buttke, Velocity methods: Lagrangian numerical methods which preserve the Hamiltonian structure of incompressible fluid flow, in *Vortex Flows and Related Numerical Methods*, edited by J. T. Beale, G. H. Cottet and S. Huberson (Kluwer, Dordrecht) 1993.
3. T. Buttke and A. Chorin, Turbulence calculation using magnetization variables, *Appl. Numer. Math.* **12**, 47–54 (1993).
4. S. G. Chefranov, The dynamics of point vortex dipoles and spontaneous singularities in three-dimensional turbulent flows, *Sov. Phys. JETP* **66**, 85 (1987).
5. M. Chen, thesis, NYU.
6. A. Chorin, *Bull. Amer. Math. Soc.* **73**, 928 (1967).
7. A. Chorin, Microstructure, renormalization, and more efficient vortex method, preprint, 1995.
8. R. Cortez, in *Proceedings of the Second International Workshop on Vortex Flows and Related Numerical Methods, Montreal, August 1995*, to appear.
9. W. E and J.-G. Liu, Vorticity boundary condition and related issues for finite difference schemes, *J. Comput. Phys.* **124**, 368 (1996).
10. W. E and J.-G. Liu, preprint, 1996.
11. W. E and C. W. Shu, A numerical resolution study of high order ENO schemes applied to incompressible flows, *J. Comput. Phys.* **110**, No. 1 (1994), 39.
12. U. Ghia, K. N. Ghia, and C. T. Shin, High-re solutions for incompressible flow using the Navier–Stokes equations and a multigrid method, *J. Comput. Phys.* **48**, 387 (1982).
13. J. Kim and P. Moin, *J. Comput. Phys.* **97**, 414 (1991).
14. V. I. Oseledets, On a new way of writing the Navier–Stokes equation. The Hamiltonian formalism, *Russ. Math. Surveys* **44**, 210 (1989).
15. C. M. Rhie and W. L. Chow, *AIAA J.* **21**, 1525 (1983).
16. R. D. Richtmyer and K. W. Morton, *Difference Methods for Initial Value Problems*, Wiley-Interscience, New York, 1967.
17. P. Roberts, A Hamiltonian theory for weakly interacting vortices, *Mathematica* **19**, 169–179 (1972).
18. R. Schreiber and H. B. Keller, Driven cavity flows by efficient numerical techniques, *J. Comput. Phys.* **49**(1983) 310–333.
19. D. Summers and A. Chorin, in *Proceedings of the Second International Workshop on Vortex Flows and Related Numerical Methods, Montreal, August 1995*, to appear.
20. R. Temam, *Arch. Rat. Mech. Anal.* **33**, 377 (1969).
21. J. van Kan, *SIAM J. Sci. Statist. Comp.* **7**, 870 (1986).